ACCSCIENCE PUBLISHING

Asian Journal of Water, Environment and Pollution

ORIGINAL RESEARCH ARTICLE

Effects of aeration position on hydrodynamics and membrane fouling in the membrane tank of an integrated wastewater treatment system

Zhi Zheng[1,2,3†], Yipeng Xuan[2†], Peng Wang[2*], Wentao Sun[2,4], Minrui Liu[2], Qiaorui Si[2], and Daolin Du[1*]

[1]Department of Environmental Ecology Research Institute, School of the Environment and Safety Engineering, Jiangsu University, Zhenjiang, Jiangsu, China

[2]Research Center of Fluid Machinery Engineering & Technology, Jiangsu University, Zhenjiang, Jiangsu, China

[3]Department of Water Science, School of Water, Energy and Environment, Cranfield University, Cranfield, Bedfordshire, United Kingdom

[4]Shandong Engineering Research Center for High-efficiency Energy Storage and Hydrogen Energy Utilization, School of Nuclear Science, Energy and Power Engineering, Shandong University, Jinan, Shandong, China

(This article belongs to the *Special Issue: Membrane and Biology-Based Wastewater Treatment Scenarios: Saudi Arabian and Global*)

[†]*These authors contributed equally to this work.*

***Corresponding authors:**
Peng Wang (pwang@ujs.edu.cn);
Daolin Du (daolindu@163.com)

Citation: Zheng Z, Xuan Y, Wang P, *et al*. Effects of aeration position on hydrodynamics and membrane fouling in the membrane tank of an integrated wastewater treatment system. *Asian J Water Environ Pollut.* 2026;23(3):026090047. doi: 10.36922/AJWEP026090047

Received: February 24, 2026

Revised: March 20, 2026

Accepted: March 24, 2026

Published online: May 14, 2026

Abstract

Aeration conditions are critical for controlling hydrodynamics and membrane fouling in membrane bioreactors (MBRs), yet the role of aeration position in integrated sewage treatment systems remains poorly quantified. This study investigates an integrated anaerobic–anoxic–oxic–MBR membrane tank using a computational fluid dynamics-population balance model with non-Newtonian rheology of the mixed liquor. Aeration positions 5–45 mm below the membrane module were evaluated for their effects on flow structure, bubble distribution, and membrane-surface shear. The model was validated against measured bubble rise velocities, with a maximum relative error of 4.67%. The results demonstrate that aeration position strongly governs the formation of high-velocity cores, low-velocity zones, and gas holdup distribution, and thus the spatial patterns of turbulent kinetic energy and gas–liquid shear on the membrane surface. Increasing the aeration position to an intermediate level enhances bottom turbulence and mixing, reduces the fraction of low-velocity regions, and alleviates sludge deposition, whereas excessively high aeration positions lead to non-uniform velocity and gas distribution and aggravated local membrane fouling. Under practical operating conditions, an intermediate aeration position also helps control local sludge concentration and floc size, thereby mitigating pore blocking development. Overall, the findings highlight aeration position as a key yet often overlooked design and operational parameter for optimizing integrated MBR performance.

Keywords: Membrane bioreactor; Non-Newtonian mixed liquor; Membrane fouling; Aeration position; Bubble dynamics

1. Introduction

Membrane bioreactors (MBRs) have been widely applied to municipal and industrial wastewater treatment owing to their compact footprint, high effluent quality, and ease of automation.[1-4] In recent years, integrated wastewater treatment units that combine conventional activated sludge processes with membrane separation have shown pronounced advantages in small- and medium-scale plants and in decentralized treatment and upgrading projects.[5,6] However, membrane fouling remains one of the key bottlenecks limiting the long-term stable operation and cost reduction of MBRs, in which hydraulic conditions and gas–liquid two-phase flow behavior play a decisive role in both the formation and mitigation of fouling.[7-9]

Among the operational parameters, aeration not only supplies dissolved oxygen to microorganisms but also induces liquid flow and turbulence through bubble rise, thereby affecting the shear stress on the membrane surface, sludge particle transport, and the accumulation of foulants on the membrane surface and within the pores.[10-12] Previous studies have shown that aeration intensity, aeration mode, and aerator configuration can significantly alter the flow field structure and gas holdup distribution in the membrane tank, and thus influence the rate of fouling development and the increase of transmembrane pressure (TMP). Kumalo *et al.*[13] found that different aeration systems in wastewater treatment plants, particularly surface aeration versus diffused aeration, lead to distinct bioaerosol emission rates. Hou *et al.*[14] found that nanobubble aeration, compared with conventional aeration and natural storage, markedly accelerates manure wastewater sanitization, enhances nitrogen retention, and reduces ammonia and nitrous oxide emissions. Meanwhile, with the advancement of computational fluid dynamics (CFD) techniques and the population balance model (PBM), CFD–PBM multiphase flow simulations have been employed to analyze bubble break-up and coalescence, local turbulent kinetic energy (TKE) distribution, and shear field characteristics in MBRs, providing quantitative tools for membrane fouling control.[15-17] Shen *et al.*[18] found that a CFD–PBM-coupled model that explicitly incorporates particle effects can accurately predict gas holdup and volumetric mass transfer coefficients in slurry bubble columns over wide ranges of gas velocity and particle concentration. Liu *et al.*[19] found that a CFD–PBM-coupled model incorporating size-dependent carbon nanotube growth kinetics can accurately simulate carbon nanotube synthesis via catalytic chemical vapor deposition in a bubbling fluidized bed and effectively reveal the effect of ethylene mole fraction on the process. Zang *et al.*[20] found that a CFD–PBM–energy minimization multi-scale hybrid model can accurately capture bubble hydrodynamics and bed expansion in pressurized bubbling fluidized beds.

However, compared to the extensive research on aeration intensity, airflow rate, and aeration modes, the role of the geometric parameter "aeration position" in integrated MBR units remains poorly understood.[21,22] In most existing studies, the vertical location of the aeration pipe is treated as a fixed design condition, and there has been little systematic analysis of its comprehensive impact on bubble trajectories, flow field distribution, sludge particle migration, and local fouling risk.[23-25] For compact integrated wastewater treatment units with limited water depth and densely packed membrane modules, even small adjustments of aeration position may significantly change the proportion of low-velocity zones near the bottom, the distribution of shear stress on the membrane surface, and the accumulation and resuspension behavior of sludge in the membrane tank, thereby affecting anti-fouling capacity and effluent quality stability.[26]

This study focuses on the membrane tank of an integrated wastewater treatment unit and develops a coupled CFD–PBM two-phase numerical model, which is validated against experimental data. On this basis, the effects of different aeration positions on flow field structure, bubble distribution, membrane-surface shear, and fouling control performance under various operating conditions are systematically investigated. By analyzing changes in mean liquid velocity, the proportion of low-velocity regions, and TKE distribution, the regulatory role of aeration position in shaping hydraulic behavior is clarified, while the responses of bubble size, gas holdup, and sludge floc characteristics reveal the associated fouling evolution mechanisms. An aeration-position "optimization window" that can simultaneously improve hydrodynamics, enhance anti-fouling capability, and maintain treatment efficiency is thereby identified, providing quantitative theoretical support and engineering guidance for the design and operational control.

2. Materials and methods

2.1. Wastewater treatment unit and membrane tank platform of membrane bioreactor

An integrated wastewater treatment system (anaerobic–anoxic–oxic + MBR) was developed in this study, as shown in Figure 1A. Influent wastewater flows from the regulating tank into the anaerobic tank, then into the anoxic tank, followed by the aerobic tank, and finally enters the MBR tank. The integrated system is designed to treat 500 $L \cdot d^{-1}$ of wastewater, and its effluent quality meets—or in some cases exceeds—the Class B limits specified in the national standard "Discharge Standard of Pollutants for Municipal

Wastewater Treatment Plant" (GB 18918-2002). Since this study focuses exclusively on the membrane tank, a three-dimensional model of the MBR tank was established using Siemens NX (UG 12.0, Siemens Digital Industries Software, Germany). The dimensions of the membrane tank were 0.34 m × 0.58 m × 0.75 m, and the membrane module measured 0.18 m × 0.326 m × 0.412 m. The spacing between adjacent membrane sheets was 48 mm, and the diameter of the membrane module header pipe was 27 mm. Three aerators were installed beneath the membrane module. Each aerator had an outer diameter of 100 mm, an inner diameter of 90 mm, and a height of 10 mm. To investigate the effect of aeration position on membrane anti-fouling performance, the vertical distance between the aerators and the bottom of the membrane module was set to 5, 15, 25, 35, and 45 mm, respectively, as shown in Figure 1C. Five vertical distances: 5, 15, 25, 35, and 45 mm (model shown in Figure 1C, the black line in the figure) were used in the simulation process.

The membrane module in the MBR tank consists of three sub-modules, providing a total of six membrane surfaces. For ease of description and analysis, these six membrane surfaces were numbered 1#–6#, as shown in Figure 1B. In the X-axis direction, two representative planes, X132.5 and X207.5, were selected. These planes are the mid-planes between membrane surfaces 2# and 3#, and between 4# and 5#, respectively. In addition, Y290 was defined as the mid-plane of the model along the Y-axis. These three characteristic planes were selected as representative sections to effectively capture variations in the flow field across different aerator positions.

2.2. Domestic wastewater monitoring

The experimental wastewater was collected from the membrane tank of the integrated wastewater treatment unit under normal operating conditions. However, due to hydrodynamic effects, poorly mixed regions may exist within the MBR tank. To avoid interference from abnormally high or low pollutant concentrations that may occur in these regions, sampling locations were selected from well-mixed zones. Therefore, to obtain samples representative of the overall rheological behavior of the wastewater in the membrane tank, a water sampler was used to collect wastewater at the intermediate liquid level. The samples were then analyzed using a rheometer (ViscoQC 300, Anton Paar, Austria) (Figure 2), yielding highly representative measurements and ensuring the accuracy and reliability of the experimental results.

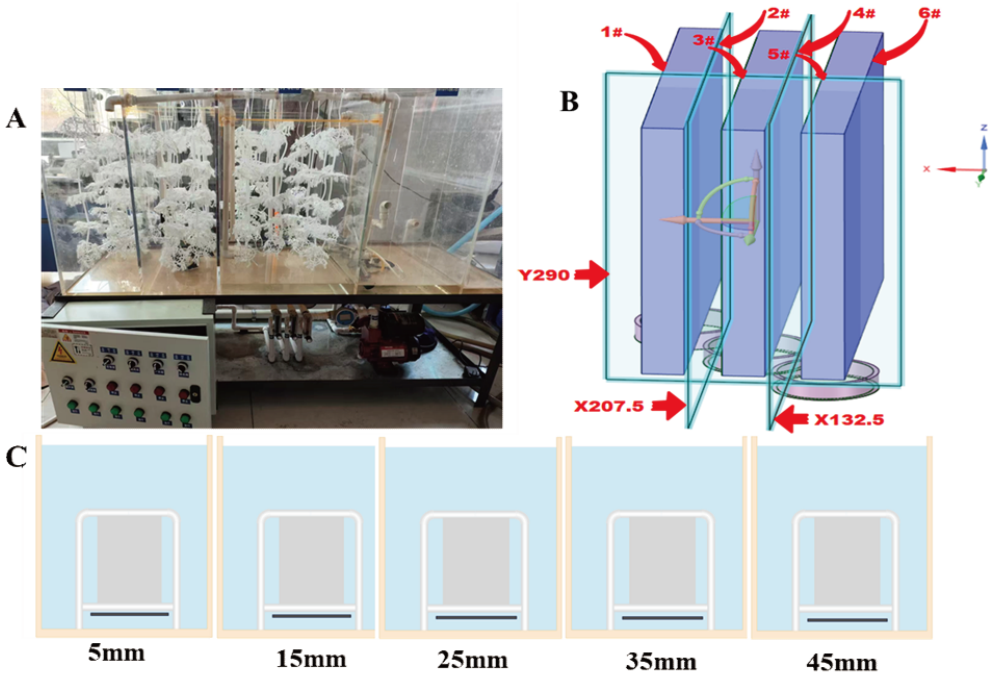

Figure 1. MBR membrane tank test bench, characteristic surface position and installation height of aeration disc. (A) Integrated wastewater treatment equipment membrane tank test bench. (B) Schematic diagram of the membrane surface and feature planes. (C) Positions of the disc diffusers relative to the bottom surface of the membrane module.

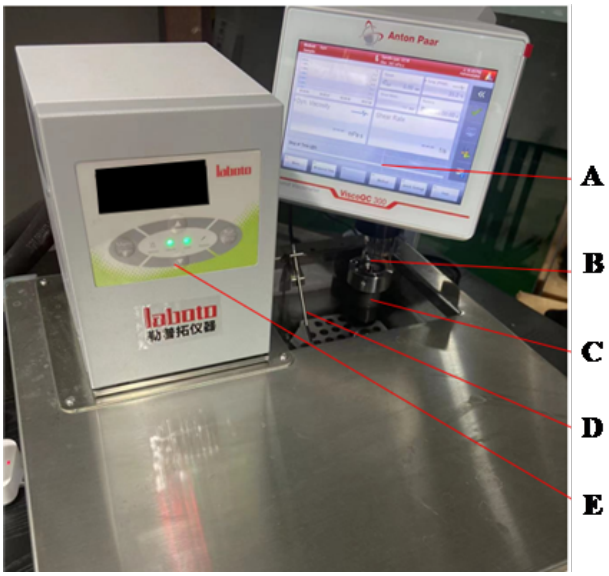

Figure 2. Schematic of the ViscoQC 300 viscometer used for sewage rheology measurements. (A) Anton Paar QC-300 rheometer. (B) CC12 rotor. (C) Small-sample adapter. (D) Temperature sensor. (E) Thermostatic water bath.

The rheological behavior of domestic sewage conforms to the Ostwald–de Waele power-law model, whose constitutive equation is given by Mehrjoo *et al.*[27] (**Equation 1**):

$$\tau = K \cdot \dot{\gamma}^{n} \tag{1}$$

where K is the consistency index (Pa·s^n), n is the flow behavior index (dimensionless), and $\dot{\gamma}$ is the shear rate (s^{-1}).

Accordingly, the relationship between apparent viscosity and shear rate can be expressed as **Equation 2**:

$$\eta = K \cdot \dot{\gamma}^{n-1} \tag{2}$$

The experimentally obtained rheological data for domestic sewage were processed and fitted using nonlinear regression. The resulting rheological curves of domestic sewage at different solid contents are shown in Figure 3.

As shown in Figure 3, variations in sewage viscosity are governed by multiple interacting factors. Domestic wastewater contains a wide range of organic substances that, during biodegradation, generate intermediate metabolites, including high-molecular-weight organics that can increase viscosity. In the biological treatment stage, intensive microbial proliferation—particularly excessive growth of filamentous bacteria—leads to the release of extracellular polymeric substances, such as polysaccharides, into the bulk liquid, thereby further elevating the viscosity. In addition, during the sludge–water separation process in the membrane tank, improper control of return sludge concentration or inadequate wasting of excess sludge increases the concentration of suspended solids in the mixed liquor, likewise resulting in a marked increase in wastewater viscosity.

The rheological parameters of domestic sewage are summarized in Table 1. As solid content increased, interactions among suspended particles, organic matter, and microorganisms intensified, raising the viscosity of the wastewater and reducing its mobility. In terms of rheological parameters, this was reflected by an increase in the consistency index K and a decrease in the flow behavior index n, indicative of more pronounced shear-thinning behavior. Consequently, the flow characteristics of the sewage deviate increasingly from those of an ideal Newtonian fluid and exhibit complex non-Newtonian rheological behavior.

2.3. Numerical simulation method

The flow of a fluid obeys the laws of conservation of mass, momentum, and energy, which can be expressed as:

(i) Continuity equation (mass conservation, **Equation 3**):[28]

$$\frac{\partial \rho}{\partial t} + \frac{\partial (\rho u)}{\partial x} + \frac{\partial (\rho v)}{\partial y} + \frac{\partial (\rho w)}{\partial z} = 0 \tag{3}$$

where ρ is the fluid density (kg·m^{-3}), t is time (s), and $\vec{u}$ is the velocity vector, with u, v, and w being the velocity components in the x, y, and z directions (m·s^{-1}), respectively.

For an incompressible fluid with constant density, **Equation 4** can be used:

$$\frac{\partial (u)}{\partial x} + \frac{\partial (v)}{\partial y} + \frac{\partial (w)}{\partial z} = 0 \tag{4}$$

(ii) Momentum conservation (**Equations 5–7**):[29]

$$\frac{\partial (\rho u)}{\partial t} + div(\rho u \vec{u}) = -\frac{\partial P}{\partial x} + \frac{\partial \tau_{xx}}{\partial x} + \frac{\partial \tau_{yx}}{\partial y} + \frac{\partial \tau_{zx}}{\partial z} + F_x \tag{5}$$

$$\frac{\partial (\rho v)}{\partial t} + div(\rho v \vec{u}) = -\frac{\partial P}{\partial y} + \frac{\partial \tau_{xy}}{\partial x} + \frac{\partial \tau_{yy}}{\partial y} + \frac{\partial \tau_{zy}}{\partial z} + F_y \tag{6}$$

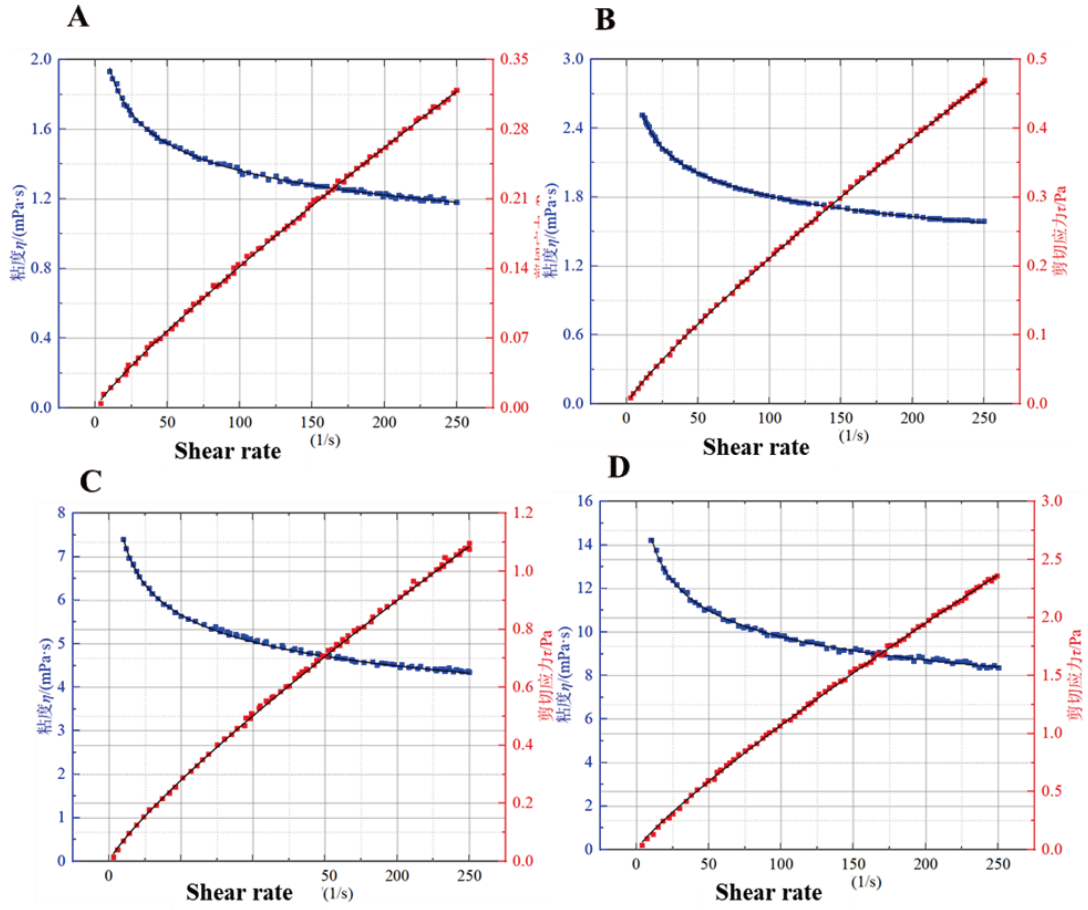

Figure 3. Rheological curve of domestic sewage with different solid content. (A) Solid content 0.13%. (B) Solid content 0.25%. (C) Solid content 0.48%. (D) Solid content 0.73%.

Table 1. Rheological parameters of domestic sewage with different solid content

Number	Solid content rate (%)	K (Pa·s^n)	*n*	η_{min} (Pa·s)	η_{max} (Pa·s)	R^2
1	0.13	0.0028	0.8651	0.0019	0.0011	0.998
2	0.25	0.0042	0.8503	0.0028	0.0017	0.998
3	0.48	0.0108	0.8330	0.0074	0.0043	0.997
4	0.73	0.0217	0.8248	0.0142	0.0083	0.997

$$\frac{\partial(\rho w)}{\partial t}+div(\rho w\vec{u})=-\frac{\partial P}{\partial z}+\frac{\partial \tau_{xz}}{\partial x}+\frac{\partial \tau_{yz}}{\partial y}+\frac{\partial \tau_{zz}}{\partial z}+F_z \quad (7)$$

where P is the static pressure (Pa), τ_{ij} is the viscous stress tensor (Pa), and F_x, F_y, F_z is the body force per unit mass (N) acting in the x, y, and z directions.

(iii) Energy conservation equation (**Equation 8**):[30]

$$\frac{\partial(\rho T)}{\partial t}+div(\rho\overline{u}T)=div\left(\frac{k}{c_p}gradT\right)+S_T \quad (8)$$

where c_p is the specific heat capacity at constant pressure (J·kg^{-1}·K^{-1}), T is the temperature (K), k is the thermal conductivity or effective heat-transfer coefficient of the fluid (W·m^{-2}·K^{-1}), and S_T is the viscous dissipation term.

In our study, the renormalization group (RNG) k-ε turbulence model was adopted.[31] Compared to the standard k-ε model, the RNG model introduces an additional term into the ε equation, which improves the prediction accuracy for high-strain-rate flows and accounts for the influence of smaller-scale eddies on turbulence. It performs better in flows with strong streamline curvature, vortices, and rotation, and can effectively capture locally complex flow structures. This provides a distinct advantage in resolving the shear-stress distribution over the membrane surface in the membrane tank of the integrated wastewater treatment system. The transport equations of the RNG k-ε model can be written as **Equations 9** and **10**:

$$\frac{\partial}{\partial t}(\rho k)+\frac{\partial}{\partial x_i}(\rho k u_i)=\frac{\partial}{\partial x_j}(\alpha_k\mu_{eff}\frac{\partial k}{\partial x_j})+G_k+G_b-\rho\varepsilon-Y_M+S_k \quad (9)$$

$$\frac{\partial}{\partial t}(\rho\varepsilon)+\frac{\partial}{\partial x_i}(\rho\varepsilon u_i)=\frac{\partial}{\partial x_j}[\alpha_\varepsilon\mu_{eff}\frac{\partial\varepsilon}{\partial x_j}]+C_{1\varepsilon}\frac{\varepsilon}{k}(G_k+C_{3\varepsilon}G_b)-C_{2\varepsilon}\rho\frac{\varepsilon^2}{k}-R_\varepsilon+S_\varepsilon \quad (10)$$

where $C_{1\varepsilon}=1.42$, $C_{2\varepsilon}=1.68$, G_k is the production of TKE due to the mean velocity gradients, G_b is the production of TKE due to buoyancy, and in compressible turbulence, the contribution from fluctuating dilatation. $C_{1\varepsilon}$, $C_{2\varepsilon}$, and $C_{3\varepsilon}$ are empirical constants; a_k and a_ε are the inverse effective turbulent Prandtl numbers for the k and ε equations, respectively; and any user-specified source terms can be incorporated through additional functions defined by the user.

At present, in the multiphase flow simulation software, ANSYS Fluent (2021R, ANSYS, Inc., USA), the Euler–Euler model provides more reliable results for strongly turbulent and persistent flows and agrees well with the aeration process, with relatively small deviations.[32-34] Therefore, the Euler–Euler multiphase flow model was adopted in this study.

The PBM takes into account the bubble size distribution and the effects of bubble coalescence and break-up on bubble size,[35] thereby overcoming the large deviations associated with the conventional single-diameter bubble model in representing the actual bubble state during aeration.[36] As a result, PBM can provide more accurate multiphase flow simulation results. Its general form can be written as **Equation 11**:

$$\frac{\partial}{\partial t}\left[n(V,t)\right]+\nabla\cdot\left[\boldsymbol{u}n(V,t)\right]=\frac{1}{2}\int_0^V c(V-V',V')n(V-V',t)n(V',t)dV'-\int_0^\infty c(V,V')n(V,t)n(V',t)dV'+\int_{\dot{U}_V} b(V')\beta(V\,|\,V')n(V',t)dV'-b(V)n(V,t) \quad (11)$$

where V is the parent-bubble volume, V' is the daughter-bubble volume, $n(V',t)$ is the number density function of daughter bubbles, $c(V-V',V')$ is the bubble coalescence rate, (V,V') is the daughter-bubble size distribution function for a parent bubble breaking into bubbles of volume V', and $b(V)$ is the bubble break-up (disintegration) frequency.

To more accurately describe the rheological behavior of complex fluids such as sewage and to obtain more precise hydrodynamic parameters, a non-Newtonian fluid model was employed. The non-Newtonian fluid considered in this study is viscous, inelastic, and incompressible. Its governing equations can be expressed as **Equations 12** and **13**:

$$d\vec{u}/dt=\vec{f}-(1/\rho)\nabla p+\Delta v\vec{u} \quad (12)$$

$$\nabla\cdot\vec{u}=0 \quad (13)$$

where t is time (s), $\vec{u}$ is the velocity vector of a fluid particle (m·s^{-1}), $\vec{f}$ is the external body force per unit mass acting on the fluid (N·kg^{-1}), ρ is the fluid density (kg·m^{-3}), p is the pressure acting on the fluid particle (Pa), and v is the effective kinematic viscosity of the non-Newtonian liquid (m^2·s^{-1}).

2.4. Model validation

The numerical simulations were conducted using ANSYS Fluent. The RNG k–ε model was selected as the turbulence model, and the Euler–Euler framework was coupled with a PBM to describe the gas–liquid multiphase flow, in which the liquid phase was treated as the continuous phase and the gas phase as the dispersed phase. The surface tension coefficient between the gas and liquid phases was set to 0.072 $N{\cdot}m^{-1}$.

The upper surface of the aerator was specified as a velocity inlet, with a gas volume fraction of one at the inlet and an initial bubble diameter range of 1–2 mm. The top boundary was defined as a degassing outlet, allowing only gas to leave the domain while prohibiting liquid discharge. The walls of the membrane tank, the membrane modules, and the lateral surfaces of the aerator were all imposed as no-slip boundaries. The flow field was solved using a pressure–velocity coupled solver, which exhibits good convergence behavior and computational efficiency for steady-state calculations. Convergence of each solution was assessed using the normalized residuals of key physical quantities, such as the cross-sectional mean velocity and mean shear stress on the membrane surface. Specifically, as the time step or iteration number increased, these residuals were required to stabilize within a small range; a residual value below 10^{-5} was taken as the convergence criterion, indicating that a statistically steady solution had been reached.

The model was validated against high-speed camera experiments to evaluate its reliability. A total of 21 sampling points were selected, and bubble velocities at different locations were obtained using PCC software from experiments conducted at an aeration velocity of 0.8 $m{\cdot}s^{-1}$. These experimental data were then compared to the corresponding simulated velocities. As shown in Figure 4, the maximum recorded relative error was 4.67%, and the discrepancies between simulated and experimental values were all within 5%, demonstrating the high reliability of the proposed model.

3. Results and discussion

3.1. Effect of aeration position on flow field and velocity under low-load operating conditions

Figure 5 shows the cloud map of velocity vector distribution at the bottom of the membrane tank. It can be seen that strip-shaped high-velocity zones appeared at both ends, and these high-velocity regions became more pronounced as the aeration position increased. This is mainly because the bottom of the membrane rack does not fully contact the tank floor, leaving a certain clearance. The narrowed space accelerates the flow when the liquid passes through it. With the increase of the aeration position, the area of the dark-blue region with a velocity close to 0 $m{\cdot}s^{-1}$ gradually decreased, and the average velocity at the bottom of the membrane tank increased accordingly. This indicates that changing the aeration position effectively activates the fluid at the tank bottom: originally stagnant liquid is subjected to sufficient stirring and mixing, thereby enhancing the anti-fouling/anti-deposition performance of the membrane tank.

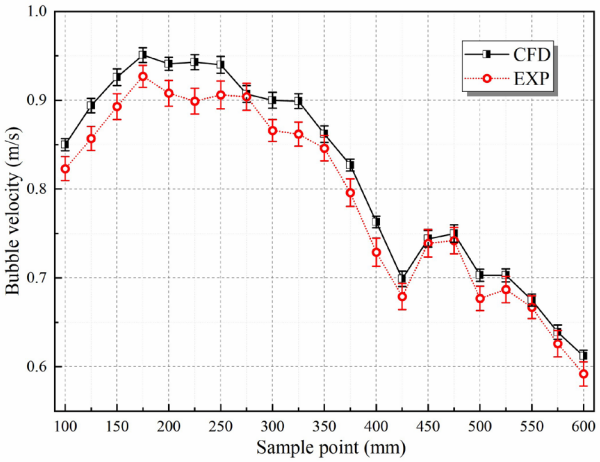

Figure 4. Comparison of the bubble velocity experiment and the numerical simulation.
Abbreviations: CFD: Computational fluid dynamics; EXP: Experimental.

Moreover, a distinct central vortex region can be observed at the bottom of the membrane tank. The formation of this central vortex is mainly attributed to rotational flow induced by aeration at the tank bottom. Such rotational flow not only promotes more uniform mixing of the bottom liquid but also exerts an effective scouring action on settled solids, further improving the resistance to sludge deposition of the membrane tank. Further analysis showed that the position of this central vortex region shifted significantly as the aeration position changed. This is primarily because the variation in aeration position alters the flow-field distribution at the tank bottom, which in turn affects the generation and location of the central vortex. This process is closely related to the velocity distribution near the bottom: changes in aeration position cause corresponding changes in the near-bottom velocity field, thereby leading to the relocation of the central vortex region.

Figure 6 presents the velocity distributions on five cross-sections at Y = 87.5 mm, 175 mm, 290 mm, 405 mm, and 492.5 mm under different aeration positions. It can

be observed that when the aeration positions were 5, 15, and 25 mm, the high-velocity zones were mainly located between membrane sheets 2# and 3#; when the aeration positions were 35 and 45 mm, the high-velocity zones were mainly located between membrane sheets 4# and 5#. Analysis shows that for aeration positions close to the membrane bottom (e.g., 5, 15, and 25 mm), bubbles were released, immediately contacted the surrounding liquid, and started accelerating upward. Because the distance to the membrane surface was relatively small, the gas energy had not yet been largely dissipated, and the bubble plume was constrained by the adjacent membrane sheets during its rise. As a result, a relatively strong convection zone was formed in the gap between membrane sheets 2# and 3#. As the aeration position increased, the rising bubbles induced more intense turbulence, thereby enhancing vertical mixing between upper and lower liquid layers. When the aeration position was increased to 35 and 45 mm, bubbles had to pass through a thicker liquid layer before reaching the free surface, which produced stronger agitation. At this stage, although the kinetic energy of bubbles was consumed more substantially, the bubbles were also pushed upward by those rising from below, causing more gas–liquid interactions to concentrate between membrane sheets 4# and 5# and forming a new turbulent core. Furthermore, a higher aeration position implies a longer rising path for the bubbles and thus greater resistance; part of the bubble energy is converted into lateral dispersion, expanding the bubble distribution range. During the ascent, bubbles near the bottom may coalesce and grow, altering the flow patterns between membrane sheets and leading to a lateral shift of the high-velocity zones.

By varying the inlet boundary condition, the aeration position was shifted from 5 mm to 45 mm, and data on each cross-section were recorded. After calculation, the gas–liquid velocity standard deviations on each plane under different aeration positions were obtained, as summarized in Table 2.

From Figure 7, it can be observed that as the aeration position decreased, the standard deviations of gas and liquid velocities on each plane increased, indicating reduced velocity uniformity. The main reason is that at a lower aeration position, the influence range of the bubbles is relatively limited, and their disturbance to the velocity field is comparatively small. However, as the aeration position is raised, the influence range of the bubbles expands, and the disturbance to the velocity distribution increases accordingly. Further analysis showed that, first, as the aeration position increased, the spatial distribution of bubbles in the liquid became more extensive. The generation and rise of bubbles entrained the surrounding liquid, inducing intense turbulence, making the velocity distribution more complex. Second, changes in aeration

Table 2. Standard deviation of air–liquid phase pairing in each plane at different aeration positions

Aeration position	Plane	S_{Water}	$\bar{V}_{Water}$	CV_{Water}	S_{Air}	$\bar{V}_{Air}$	CV_{Air}
5 mm	X132.5	0.2132	0.3422	62.30%	0.3322	0.4504	73.76%
	X207.5	0.2083	0.3352	62.14%	0.3171	0.4344	73.00%
	Y290	0.2183	0.3765	57.98%	0.3388	0.6270	54.04%
15 mm	X132.5	0.2211	0.3461	63.88%	0.3452	0.4542	76.00%
	X207.5	0.2145	0.3396	63.16%	0.3394	0.4500	75.42%
	Y290	0.2302	0.3840	59.95%	0.3586	0.6326	56.69%
25 mm	X132.5	0.2410	0.3532	68.23%	0.3620	0.4623	78.30%
	X207.5	0.2264	0.3525	64.23%	0.3542	0.4585	77.25%
	Y290	0.2379	0.3843	61.90%	0.3693	0.6343	58.22%
35 mm	X132.5	0.2480	0.3565	69.57%	0.3666	0.4580	80.04%
	X207.5	0.2449	0.3592	68.18%	0.3671	0.4682	78.41%
	Y290	0.2481	0.3957	62.70%	0.3774	0.6461	58.41%
45 mm	X132.5	0.2531	0.3581	70.68%	0.3887	0.4700	82.70%
	X207.5	0.2508	0.3636	68.98%	0.3874	0.4841	80.02%
	Y290	0.2549	0.3927	64.91%	0.3883	0.6524	59.52%

Abbreviation: CV: Coefficient of variation.

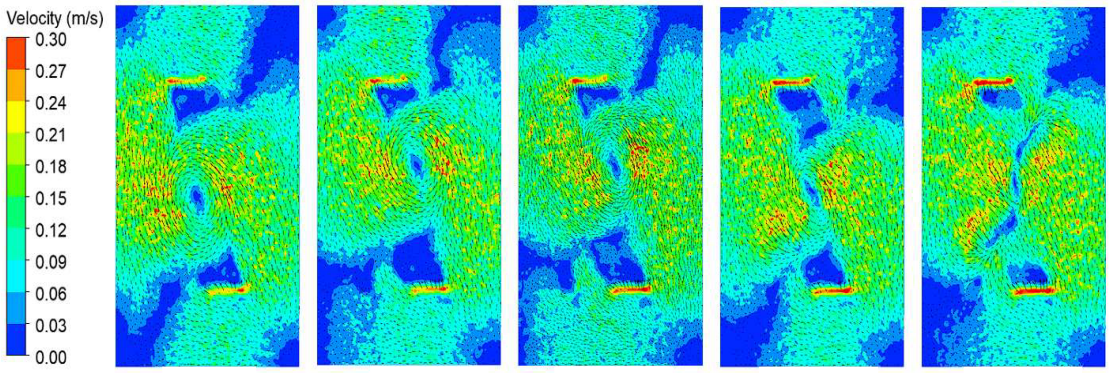

Figure 5. Cloud map of the speed distribution of the membrane tank at different aeration positions

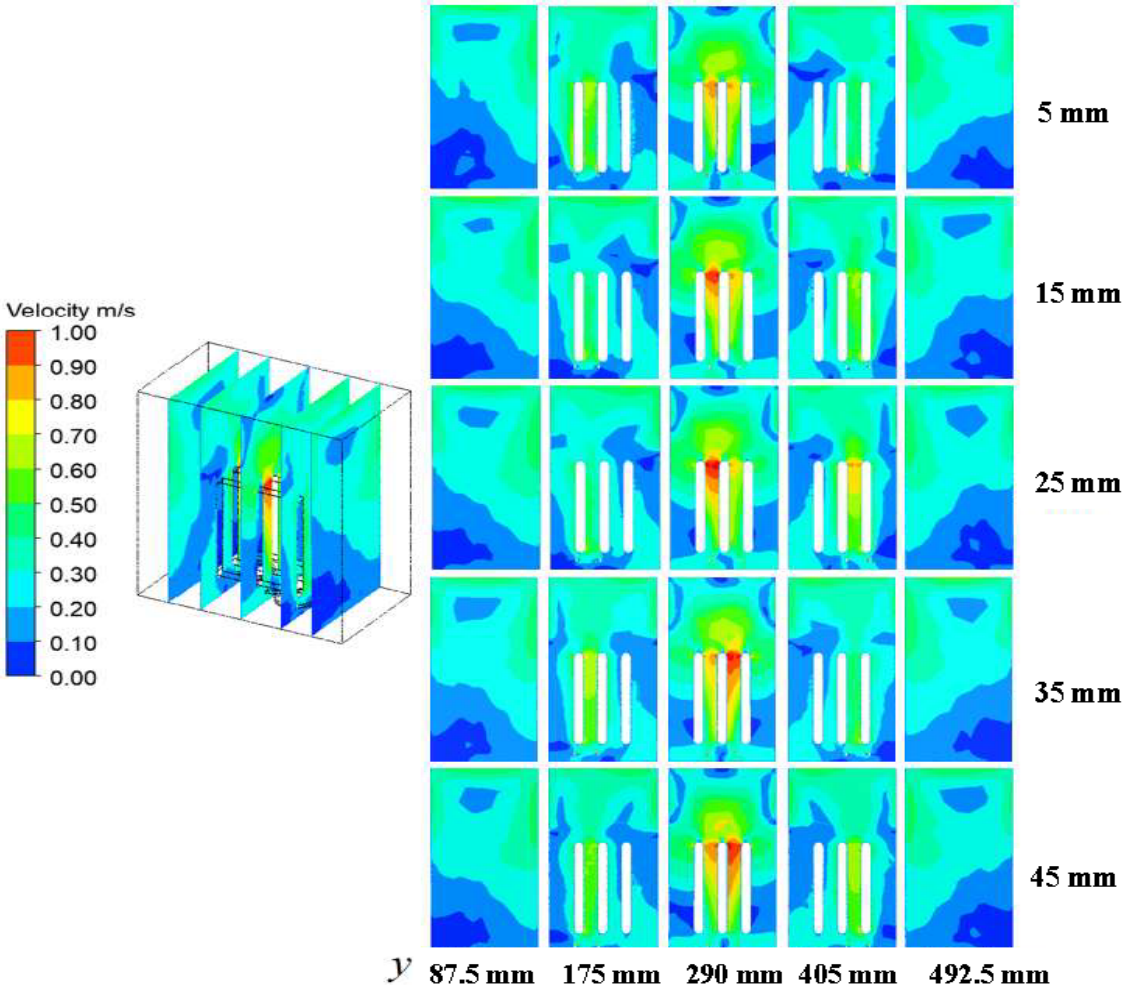

Figure 6. Cloud map of the speed distribution of each plane at different aeration speeds

position also affected the bubble rise velocity and spatial number density, thereby influencing the uniformity of the velocity field.

Figure 8 indicates that, as the aeration position increased, the average gas and liquid velocities inside the membrane tank first increased and then decreased, although the variation amplitude was relatively small. This trend can be explained as follows: when the aeration position is relatively low, it produces strong agitation of the liquid near the bottom of the membrane tank, significantly increasing the local liquid velocity in the lower region and thus raising the overall average velocity in the tank. However, an excessively high aeration position may cause markedly high local velocities in certain regions while other areas remain under-circulated. Because the gas phase is not sufficiently dispersed and mixed throughout the entire tank during its ascent, the regions near the bottom exhibit relatively high velocities, whereas the upper layer or regions far from the aeration point lack an effective driving force and therefore have relatively low velocities. As a result, the overall average velocity in the membrane tank decreases compared to the previous condition.

3.2. Effect of aeration position on bubble distribution under low-load operating conditions

Figure 9 shows that the mean bubble diameter increased with increasing aeration position. When the aeration position was 5 mm, the mean bubble diameter was 3.477 mm; at 15 mm, the mean diameter was 3.486 mm, an increase of 0.26%; at 25 mm, it increased to 3.500 mm, i.e., 0.40% higher. When the aeration positions were 35 mm and 45 mm, the mean bubble diameters reached 3.548 mm and 3.710 mm, corresponding to increases of 1.37% and 4.57%, respectively, compared to the preceding condition.

This is mainly because the hydrostatic pressure of the water column increases at deeper aeration positions, reducing the net buoyancy (the difference between buoyancy and gravity) acting on the bubbles and thus slows their rise velocity. The prolonged residence time of bubbles in the liquid phase provides more opportunity for bubble–bubble coalescence and for deformation/stretching by the surrounding flow, thereby increasing the mean bubble diameter. In addition, when aeration is applied at greater depths, a higher pressure head must be overcome to

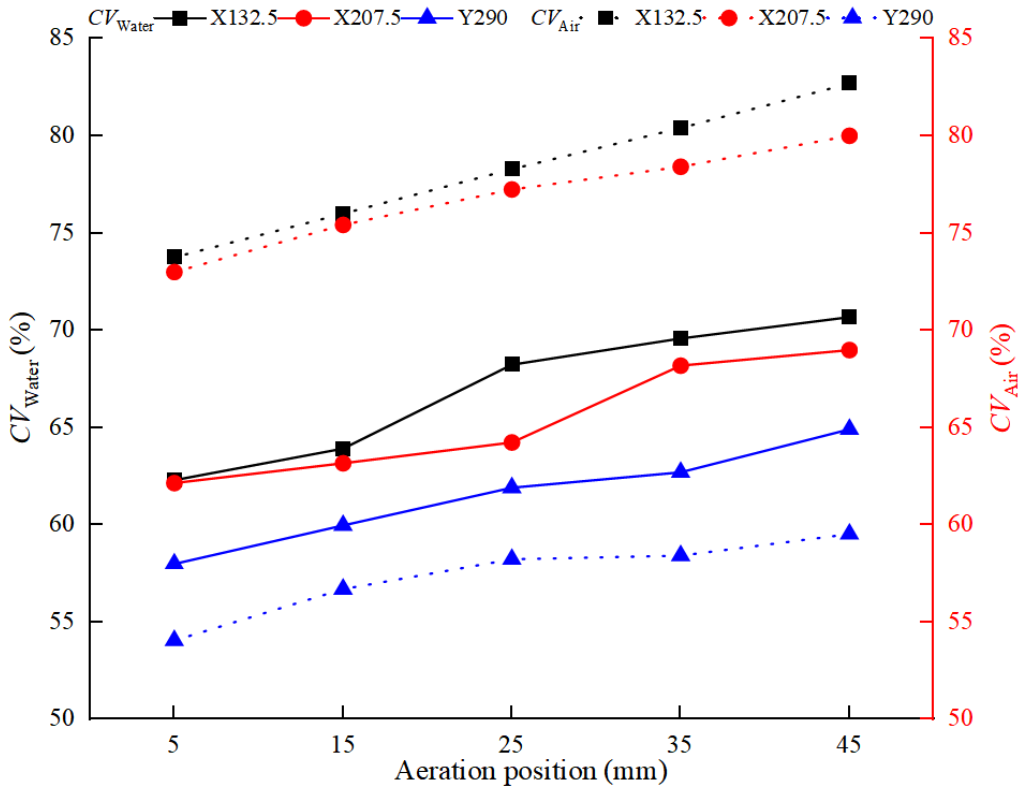

Figure 7. Variation of velocity uniformity in each plane at different aeration positions
Abbreviation: CV: Coefficient of variation.

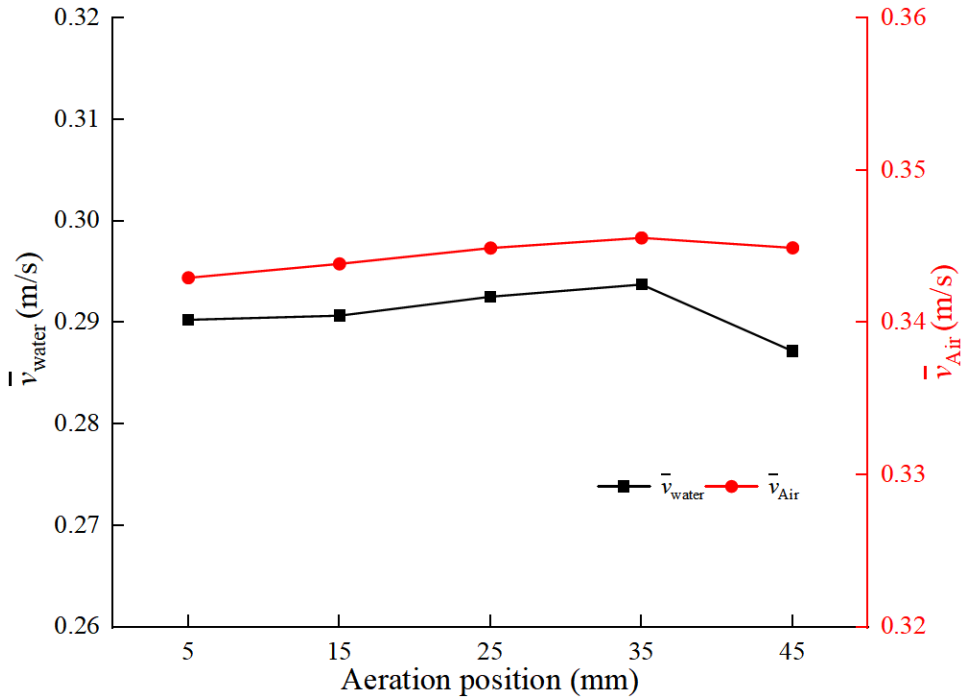

Figure 8. Change of average velocity of the membrane tank at different aeration positions

effectively disperse the gas throughout the water column; this tends to reduce the uniformity of gas dispersion and promote the formation of larger-diameter bubbles.

Figure 10 illustrates the variation in gas holdup in the membrane tank as a function of aeration position. When the aeration position was 5 mm, the gas holdup was 2.64%; at 15 mm, the gas holdup increased to 2.69%, i.e., by 1.89%; at 25 mm, it reached 2.74% (an increase of 1.86%); at 35 mm, it further increased to 2.79% (an increase of 1.82%). However, when the aeration position was 45 mm, the gas holdup decreased to 2.56%, a 8.24% reduction. The initial increase is attributed to the extended residence time of bubbles in the water as the aeration depth increases, enhancing the opportunity for gas dissolution. Turbulent diffusion combined with convective transport promotes a more uniform distribution of gas within the liquid, thereby increasing gas holdup in the membrane tank. Nevertheless, when bubble diameters become excessively large, the oxygen dissolution rate within individual bubbles decreases. Although the volume of a single bubble increases, the number of bubbles per unit volume decreases, and the specific gas–liquid interfacial area declines, leading to lower oxygen transfer efficiency and, ultimately, a decline in gas holdup.

Further numerical simulations indicated that changes in aeration position significantly affected the distribution of bubble size classes. As shown in Figure 11, at an aeration position of 45 mm, the proportion of bubbles with diameters smaller than 1.5 mm was relatively low, whereas the fractions in the > 1.5 mm-diameter classes were comparatively high. This is because gas released from deeper locations is initially strongly constrained by the surrounding water. As the bubbles rise toward the free surface, the external hydrostatic pressure gradually decreases, which enhances the tendency of gas molecules inside the bubbles to diffuse outward, leading to bubble expansion. In the absence of sufficient mixing and break-up, this expansion effect is more pronounced, resulting in a higher proportion of larger bubbles.

3.3. Effect of aeration position on anti-fouling performance under low-load operating conditions

Figure 12 shows the TKE contour plots at different aeration positions. It can be seen that, as the aeration position increased from 5 mm to 45 mm, the TKE near the bottom of the membrane tank gradually intensified. This is because aeration positions closer to the tank floor generate bubbles whose upward motion induces stronger disturbance to the sludge accumulated at the bottom. As a result, local high-velocity zones are formed, and the bottom sludge is more effectively resuspended and incorporated into the overall circulation and mixing within the membrane tank. Consequently, both the mass transfer efficiency in the tank

and the biological activity of the sludge are enhanced.

Figure 13 illustrates the effect of aeration position on the gas-phase shear stress acting on the membrane surface. The closer the aeration position was to the lower end of the membrane rack, the stronger the local gas–surface shear at the lower part of the membrane sheets. This is mainly because, in the initial stages of bubble release and expansion, bubble velocity increases rapidly, giving rise to localized, transient high-velocity flows that reinforce the shear stress. In regions farther away from the aeration point, the absence of direct bubble impingement results in weaker shear and correspondingly lower flow velocities. This no-nuniformity may cause pronounced differences in scouring intensity over the membrane surface, leaving some areas insufficiently cleaned and thereby increasing the risk of membrane fouling.

As shown in Figure 14, although the distribution of mean shear stress along the membrane surface under a given aeration position generally followed a pattern of first increasing and then decreasing, the location of the maximum shear stress varied with aeration position. Specifically, when the aeration positions were 5, 15, and 25 mm, the maximum mean shear occurred on membrane surface 3#, whereas at aeration positions of 35 and 45 mm, it shifted to membrane surface 4#. This is likely due to the lateral displacement of the high-velocity core region. Comparative analysis further indicated that the trends in mean liquid-phase and gas-phase shear stresses were consistent across all aeration positions: with increasing aeration position, the mean shear stresses exerted by both liquid and gas on the membrane surfaces exhibited an overall increasing trend.

3.4. Effect of aeration position on flow field and velocity under high-load operating conditions

Under typical conditions, when the flow velocity in the membrane tank falls below 0.1 $m \cdot s^{-1}$, mixing performance may deteriorate, and sludge deposition is likely, thereby increasing the risk of membrane fouling. According to the distributions of low-velocity regions in the membrane tank at different aeration positions shown in Figure 15, these low-velocity zones were mainly located near the bottom corners of the tank. Statistical analysis of the local velocities in the membrane tank showed that, at an aeration position of 5 mm, the proportion of low-velocity regions was 13.25%; at 15 mm, it was 12.71%; at 25 mm, 12.60%; at 35 mm, 12.20%; and at 45 mm, 12.38%.

In the membrane tank, if the near-bottom flow velocity is excessively low, activated sludge readily settles, forming a high-concentration sludge layer. This not only increases the risk of membrane fouling but may also inhibit local microbial activity, thereby impairing the overall biological treatment performance. According to the velocity–vector contour plots at different aeration positions shown in Figure 16, as the aeration position increased, the single-

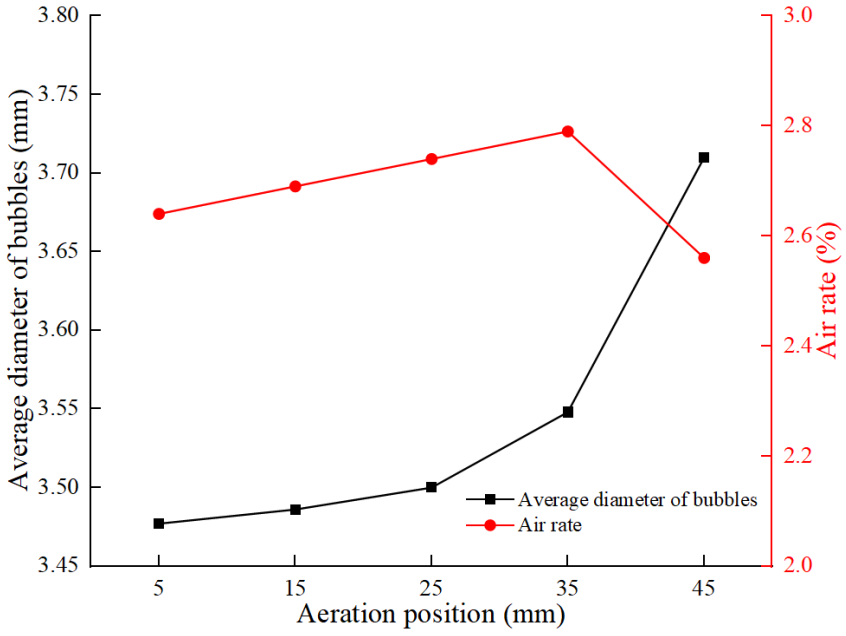

Figure 9. Plot of average bubble diameter and gas content at different aeration positions

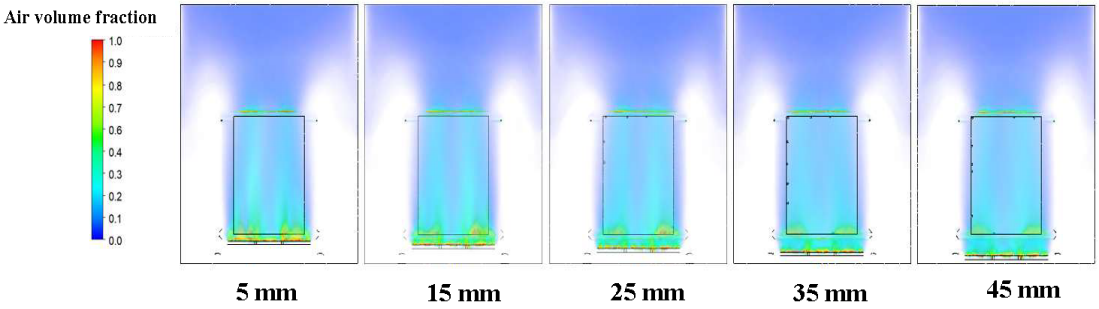

Figure 10. Distribution diagram of gas content at different aeration positions

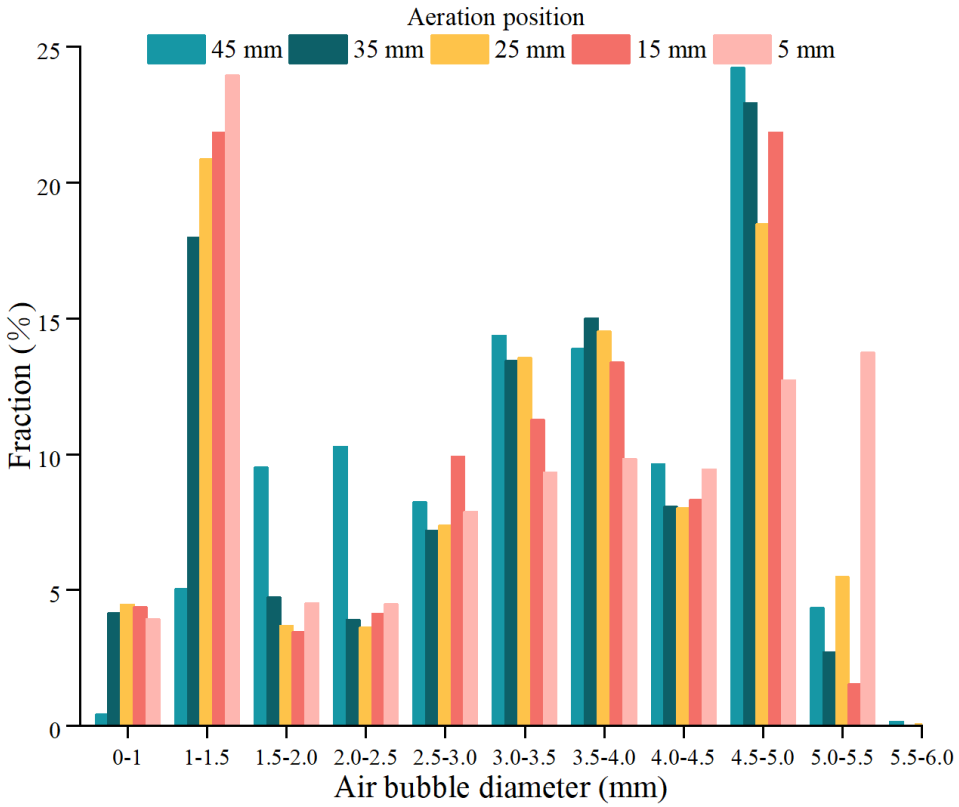

Figure 11. Statistical histogram of different bubble diameters with aeration position

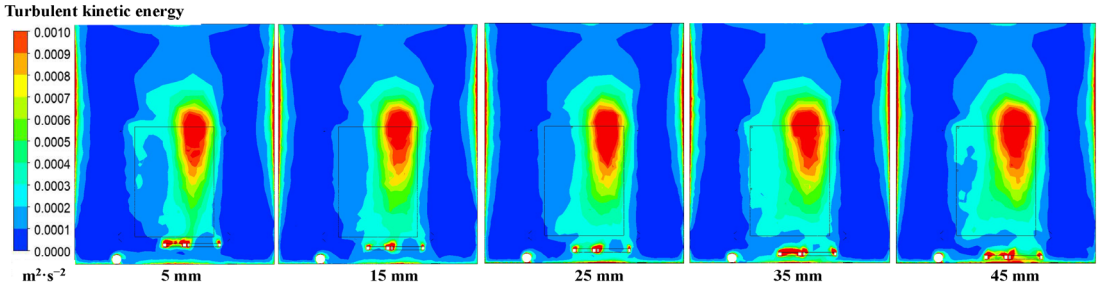

Figure 12. Cloud map of turbulent kinetic energy distribution at different aeration positions

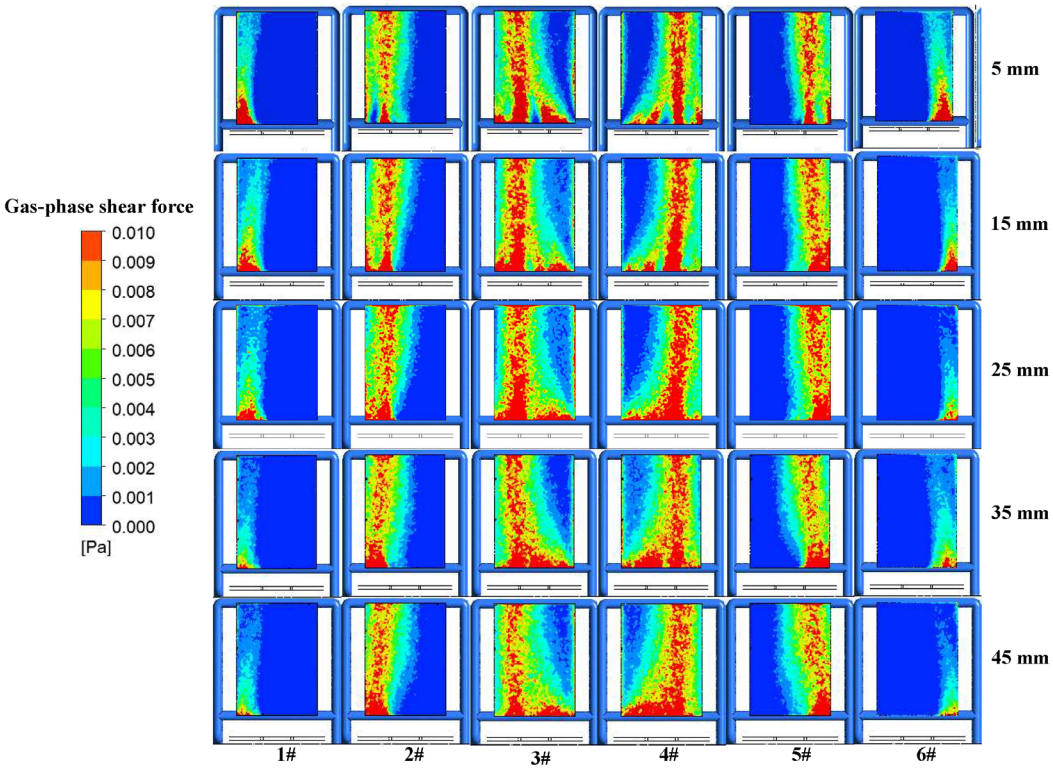

Figure 13. Cloud diagram of gas-phase shear force distribution at different aeration positions

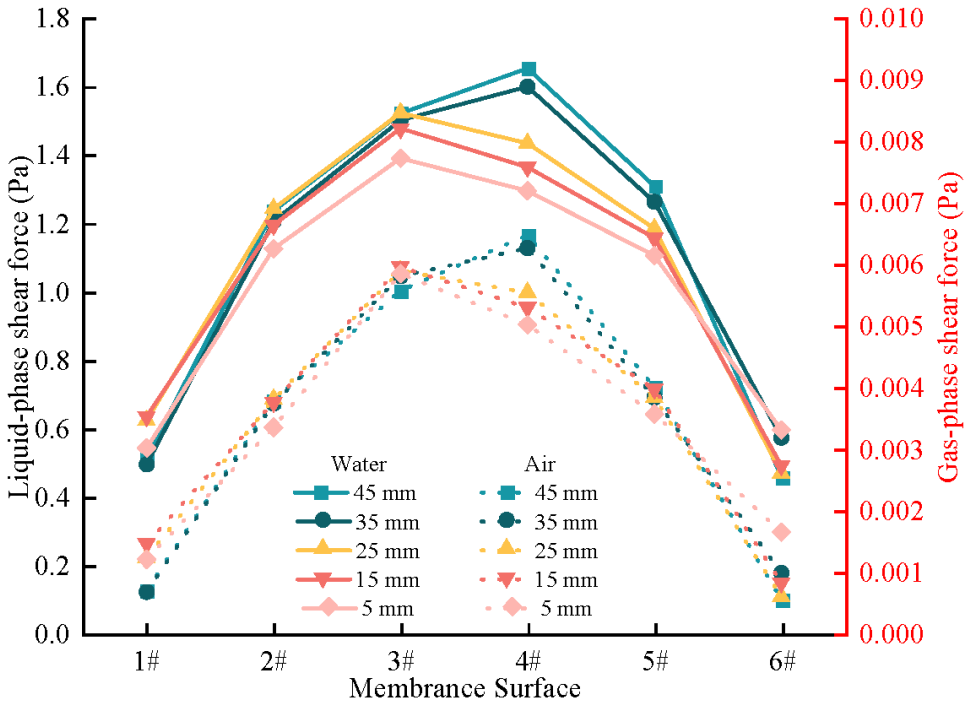

Figure 14. Average shear force distribution of the membrane surface under different aeration positions

ring central vortex at the bottom of the membrane tank gradually evolved into a threering central vortex, and the area of the highvelocity zone expanded accordingly. This transformation is conducive to the formation of upward flows, intensifying gas–liquid contact, enhancing the circulation of wastewater throughout the membrane tank, and thus preventing the buildup of settled sludge layers.

Figure 17 presents the variation of average velocity in the membrane tank under different aeration positions. When the aeration position increased from 5 to 45 mm, both the gas-phase and liquid-phase average velocities exhibited a trend of first increasing and then decreasing, similar to the low organic-loading condition; however, the variation amplitudes were relatively small. The change in average liquid velocity remained within 3%, while that of the gas phase remained within 4%. This is because increasing the aeration position expands the influence range of the bubbles, thereby enhancing gas–liquid mixing and promoting higher flow velocities within the membrane tank. Nevertheless, when the aeration position was at 45 mm, the hydraulic resistance experienced by both the gas and the liquid increased, and the bubble energy was gradually dissipated and dispersed. As the driving force weakened, the mixing and lifting effects on the upper liquid layer in the tank diminished, leading to a decrease in the average velocities of both liquid and gas within the membrane tank.

3.5. Effect of aeration position on bubble distribution under high-load operating conditions

Figure 18 shows that during aeration, increasing the aeration position altered the liquid flow and mixing, resulting in a more non-uniform liquid-velocity field. This, in turn, affected bubble-rise velocity and trajectories, thereby influencing bubble formation and size, and ultimately increasing the mean bubble diameter as a function of aeration position. In addition, as the aeration position increased, the turbulence intensity in the upper part of the membrane tank was relatively low; therefore, bubbles were less likely to break, and larger, more stable bubbles were more likely to form. Although the mean bubble diameter showed an increasing trend, its range of variation remained relatively limited compared to the clear-water case.

As an important operating parameter in the membrane tank, the aeration position directly affects the gas holdup. As shown in Figure 19, the deeper the aeration position, the more uniformly the gas was distributed in the membrane tank, and the more fully it contacted the bulk liquid; consequently, gas diffusion and mixing were enhanced, and mass-transfer efficiency was improved. However, when the aeration position was further increased to 45 mm, the gas holdup in the membrane tank gradually decreased. This is because gas diffusion is increasingly hindered by liquid flow, and local vortices and short-circuit flows are induced, leading to non-uniform gas distribution and reduced mass-transfer efficiency.

3.6. Effect of aeration position on anti-fouling performance under high-load operating conditions

From the TKE contour plots at different aeration positions in Figure 20, it can be seen that when aeration was applied at greater depths, bubbles generated from gas released from the bottom experienced higher hydrostatic pressure from the overlying water during their ascent. Under these conditions, bubble break-up releases more energy, thereby generating more intense turbulence. In addition, deep aeration improves mixing throughout the water column, prevents sludge accumulation at the bottom, promotes effective circulation of the bulk liquid, and enhances vertical fluid recirculation. As a result, the overall TKE increased, turbulence in the tank became more vigorous, and energy transfer and mixing efficiency were improved, mitigating membrane fouling.

Figure 21 shows the distribution of mean shear stress on the membrane surface under different aeration positions.

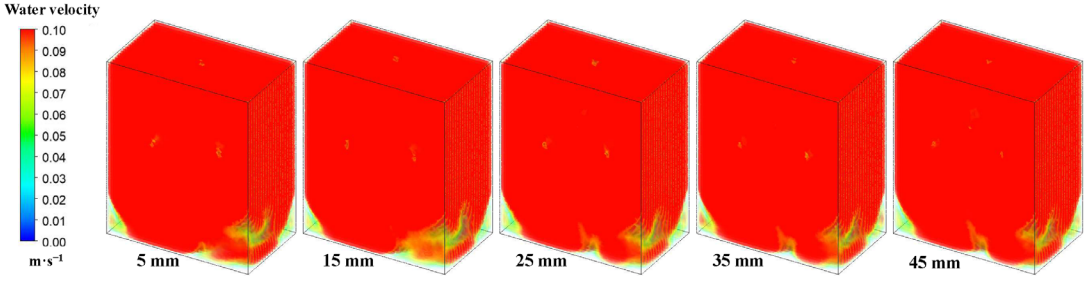

Figure 15. Distribution diagram of the low-speed area of the membrane tank at different aeration positions

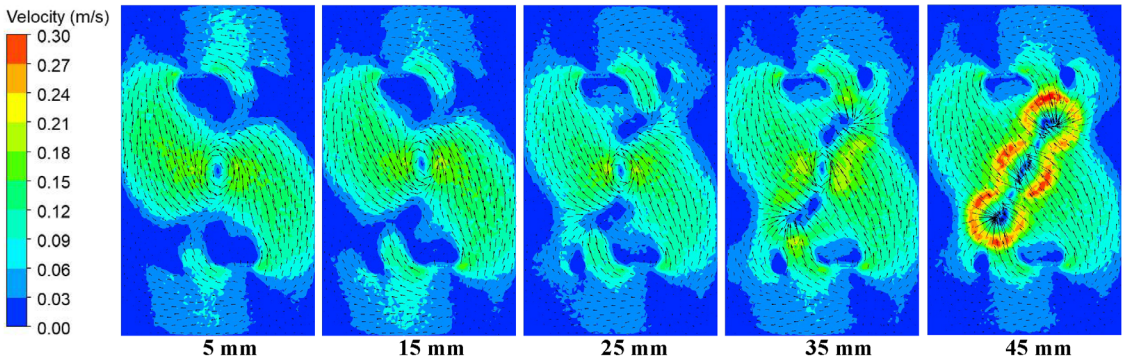

Figure 16. Cloud map of the speed distribution of the membrane tank at different aeration positions

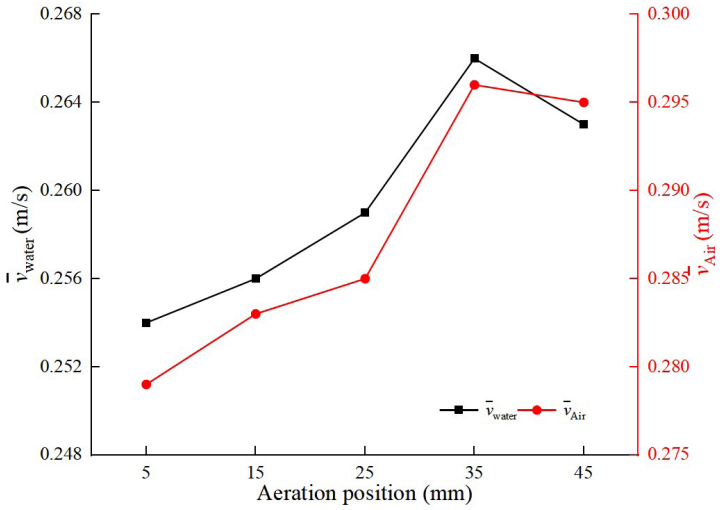

Figure 17. Plot of the average velocity change of the membrane tank under different aeration positions

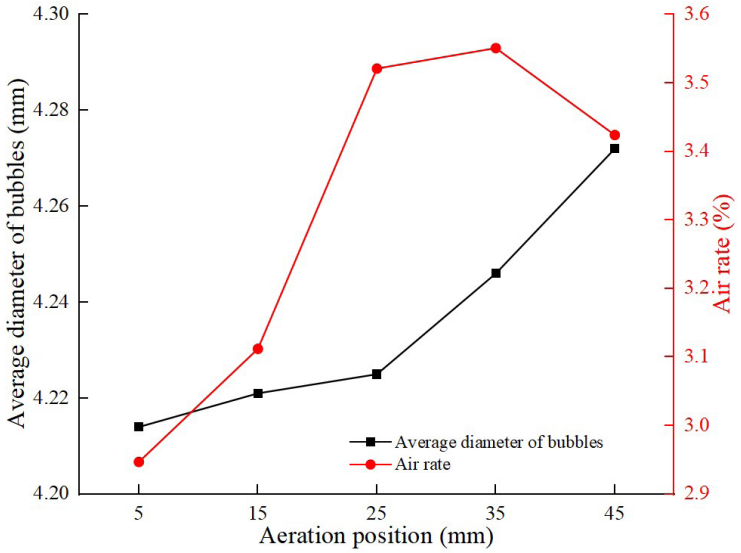

Figure 18. Plot of average bubble diameter and gas content at different aeration positions

As the aeration position was gradually deepened, the path length that the gas had to travel through the water layer increased accordingly. This change not only affected the trajectory of gas reaching the membrane surface but also substantially affected the velocities of both gas and liquid. When the aeration position was 5 mm, the gas could pass directly and rapidly through a relatively short water layer to contact and mix with the liquid; in this case, the gas and liquid velocities were relatively low, and the shear stress acting on the membrane surface was correspondingly small. However, as the aeration position was deepened, the gas had to traverse a thicker water layer before reaching the membrane surface, resulting in a longer mixing time with the liquid. This led to a gradual increase in the velocities of both phases. The increase in gas and liquid velocities enhanced frictional interaction with the membrane surface, directly resulting in higher mean shear stress.

3.7. Effect of aeration position on flow characteristics in the membrane tank under practical operating conditions

Figure 22 illustrates the variation of bubble distribution on the membrane surface with aeration position. There was a dynamic relationship between bubble behavior and aeration position. In the initial release stage, newly generated bubbles exhibited rapid formation and pronounced expansion. During this period, regions near the membrane surface experience substantially enhanced local flow, forming transient high-velocity zones. Such transient high-velocity effects exerted a strong scouring action on the membrane surface, effectively preventing pore blockage and thereby improving membrane filtration efficiency. At the same time, the formation of high-velocity regions facilitated oxygen transfer toward the membrane surface and enhanced oxygen utilization efficiency. As the aeration position increased, the released gas must travel a longer vertical distance before reaching the membrane surface. During its ascent, the bubbles traversed a longer path in the water column, allowing more time and space for thorough mixing with the liquid and for lateral dispersion. This enhanced dispersion reduced the number of bubbles impinging on a unit area of the membrane, and thus the bubble coverage density on the membrane surface declined.

3.8. Effect of aeration position on membrane fouling under practical operating conditions

Practical operation shows that foulant deposition during wastewater treatment typically proceeds through three main stages, as depicted in Figure 23. The first stage is pore-blocking fouling. Driven by the suction of the permeate pump, fine particulates in the wastewater strongly interact with the membrane elements. A portion of these particles penetrates the membrane pores and deposits within them or at the pore entrances, thereby blocking the flow channels. As a consequence, the effective pore size decreases, filtration resistance increases, and the TMP rises. This stage is primarily governed by the properties of the foulants, the characteristics of the membrane material, and the operating conditions. The second stage is gel-layer fouling. Dissolved solutes in the mixed liquor—such as macromolecular organics, proteins, and polysaccharides—are deposited on the membrane surface via physical adsorption, hydrogen bonding, and electrostatic interactions, forming a relatively loose but sticky gel-like layer. In this stage, TMP increases slowly and is therefore also referred to as the slow-fouling stage. The presence of a gel layer increases the masstransfer resistance between the membrane and

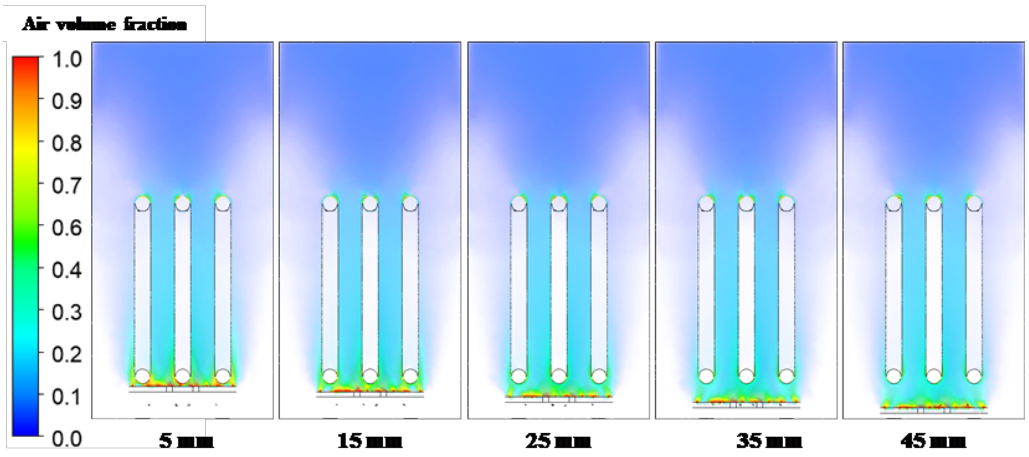

Figure 19. Distribution diagram of gas content at different aeration positions

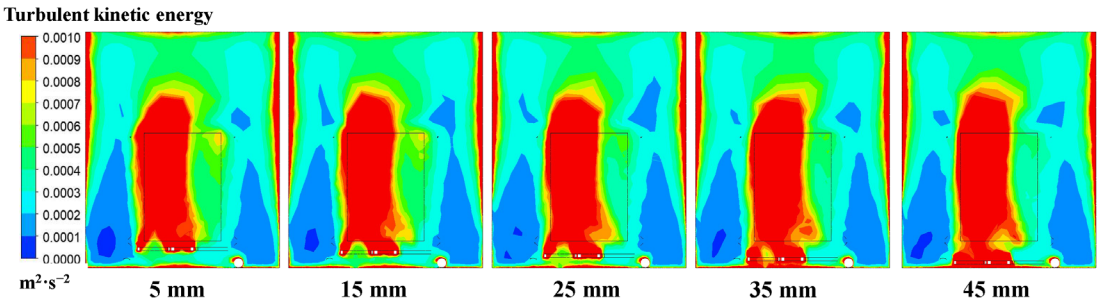

Figure 20. Cloud map of turbulent kinetic energy distribution at different aeration positions

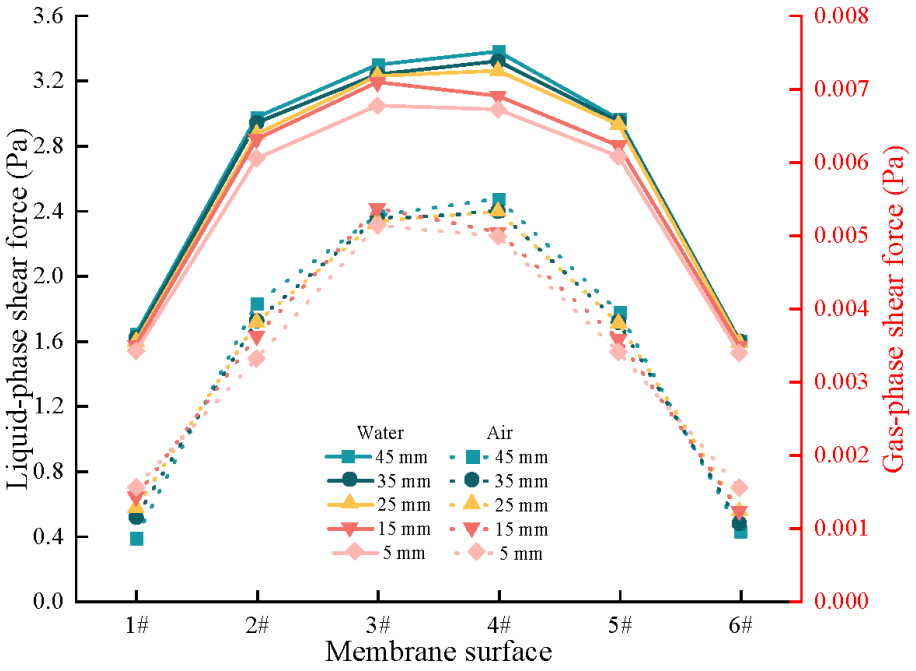

Figure 21. Average shear force distribution of the membrane surface under different aeration positions

the bulk solution. With continued operation, these solutes are repeatedly adsorbed, diffused, and desorbed, while simultaneously capturing and enriching other foulants, thereby accelerating the subsequent formation of the cake layer. The third stage is cake-layer fouling. When the concentration of suspended particles in the feed is high, or the filtration time is sufficiently long, a relatively dense and structurally stable solid layer—commonly referred to as the "cake layer"—forms on the membrane surface. This layer is typically composed of larger particles, flocculated or precipitated solids, and particles captured in the pre-existing gel layer. Owing to its low porosity, the cake layer markedly increases the overall resistance at the membrane surface, leading to a sharp decline in permeate flux and an abrupt rise in TMP. In addition, the formation of a cake layer can induce non-uniform local pressure distribution, which greatly reduces the efficiency of the membrane module and may even render it inoperable.

During the experiments, it was observed that when the aeration position was set at 5 mm, bubbles released from the bottom rose rapidly to the free surface and formed dense bubble plumes; however, their scouring effect on the membrane surface was insufficient because of relatively low impact intensity, resulting in incomplete removal of deposited foulants. Under these conditions, part of the activated sludge accumulated at the tank bottom, impairing mixing and suspension of the lower sludge layer and increasing sludge thickness beneath the membrane modules, thereby adversely affecting filtration

performance. Meanwhile, the nearby settled sludge readily formed a cake-layer type fouling.

When the aeration position was adjusted to 35 mm, gas–liquid mixing was significantly improved. Under the same operating time, the degree of membrane fouling was the lowest, indicating that this aeration position effectively prevented sludge accumulation, reduced the formation of large sludge agglomerates, and lowered the risk of sludge particles covering the membrane surface.

However, when the aeration position was further increased to 45 mm, the flow velocity in certain local regions decreased, weakening gas–liquid circulation. As a result, dissolved oxygen tended to accumulate excessively near the bottom of the membrane tank, while the upper region suffered from oxygen deficiency. This directly affected the metabolic activity of microorganisms and the pollutant removal performance. Consequently, foulant deposition and accumulation on the upper part of the membrane surface became more severe, intensifying membrane fouling, increasing the risk of pore blockage, and ultimately compromising the overall stability and longterm operability of the system.

3.9. Effect of aeration position on treatment performance under practical operating conditions

During the experiments, the mean sludge floc size under different aeration positions was measured, and its impact on sludge settleability was investigated. As shown in Figure 24, when the aeration position was 5 mm, the mean sludge particle size D_v was 278 μm. At this point, the sludge exhibited poor settling performance: part of the activated sludge could not be effectively maintained in suspension, and the resulting sludge flocs were excessively compact, with phenomena such as flotation or excessive settling, which adversely affected flocculation performance and solid–liquid separation.

As the aeration position increased, the residence time of bubbles near the bottom of the membrane tank increased, leading to higher average gas- and liquid-phase velocities. Therefore, larger sludge particles or flocs were more readily broken up into smaller ones. Consequently, when the aeration position was increased to 15 mm, the mean sludge particle size D_v decreased to 244 μm, a reduction of 8.96%. Similarly, when the aeration position was further increased to 25 mm and 35 mm, the mean

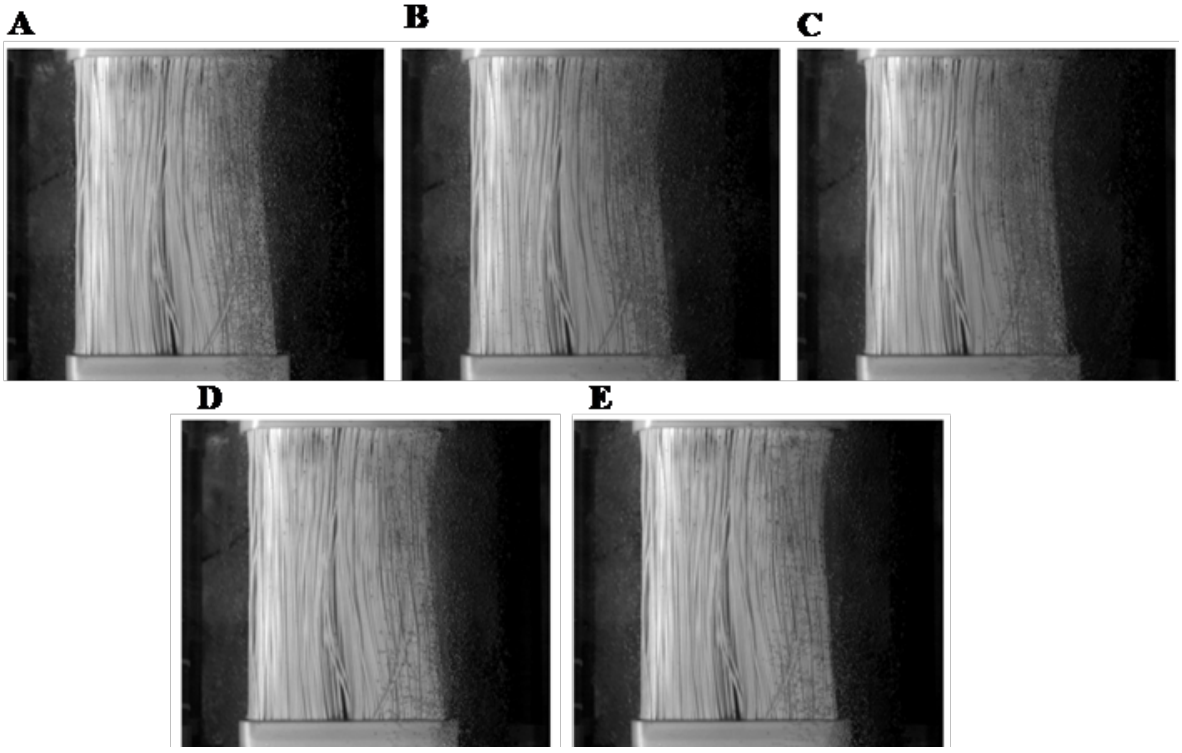

Figure 22. Schematic diagram of the bubble distribution of the membrane surface with the aeration position. (A) 5 mm. (B) 15 mm. (C) 25 mm. (D) 35 mm. (E) 45 mm.

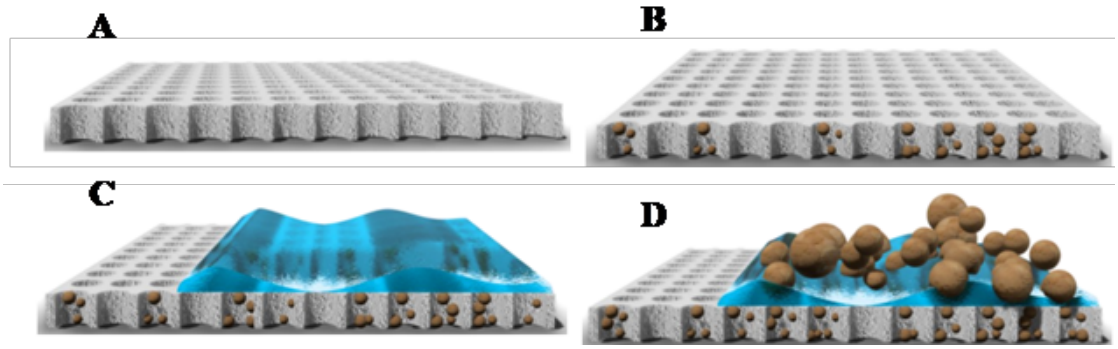

Figure 23. Schematic diagram of the surface contamination of the membrane tank. (A) No fouling. (B) Pore-blocking fouling. (C) Gel-layer fouling. (D) Cake-layer fouling.

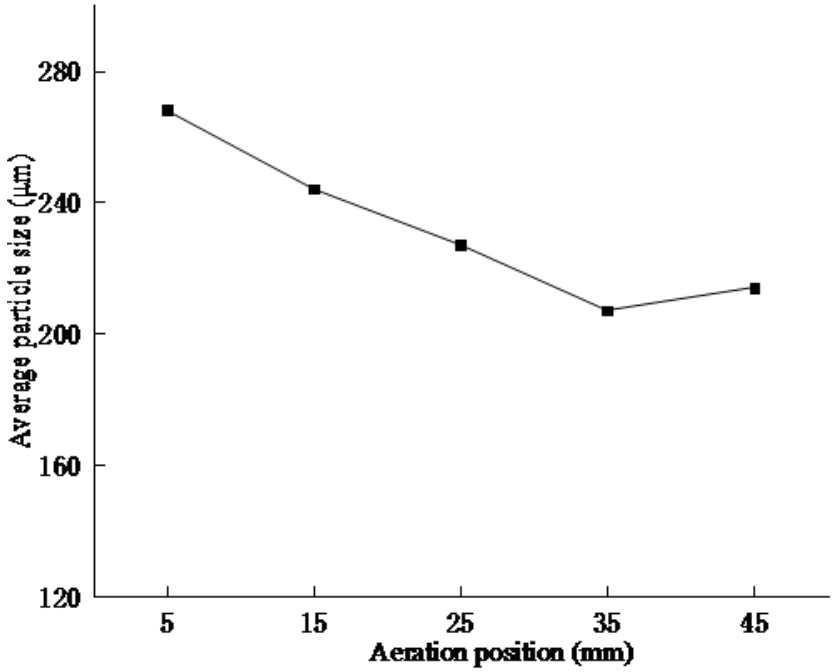

Figure 24. The average particle size of sludge under different aeration speeds

sludge particle size continued to decrease to 227 μm and 207 μm, corresponding to reductions of 6.97% and 8.81%, respectively.

However, when the aeration position was increased to 45 mm, the mean sludge particle size D_v slightly increased to 214 μm, representing a 3.38% increase. This may be because, at an aeration position of 45 mm, the average liquid and gas velocities in the membrane tank were lower than at 35 mm, resulting in locally elevated sludge concentrations farther from the aerator. Under these circumstances, part of the sludge tended to form more compact and stable flocs, leading to a slight increase in the mean sludge particle size.

4. Conclusion

This study employed a coupled CFD–PBM gas–liquid two-phase model, together with experimental observations, to clarify the influence of aeration position (5–45 mm below the membrane module) on hydrodynamics, membrane anti-fouling performance, and sludge behavior in an integrated MBR. The aeration position was identified as a key operational parameter that fundamentally governs flow structure, bubble distribution, and shear conditions on the membrane surface in an integrated MBR. This range provides the best balance between minimizing dead zones, maintaining uniform gas distribution, and

enhancing membrane surface shear. The fraction of low-velocity zones first decreased and then slightly increased as the aeration position increased. This confirms that intermediate positions are most effective at suppressing sludge deposition, while positions that are too shallow or too deep are less efficient. While deeper aeration positions increased turbulence and membrane shear force (beneficial for foulant detachment), excessively deep positions proved detrimental. They intensified the bubble-flow interaction, leading to vortices, gas short-circuiting, uneven gas holdup, and reduced local mass transfer efficiency.

Acknowledgments

None.

Funding

This study was supported by the National Key Research and Development Program of China (2022YFC3204603), the Senior Talents Fund of Jiangsu University (Project No. 20JDG39), and the Postgraduate Research and Practice Innovation Program of Jiangsu Province (KYCX24_4002).

Conflict of interest

The authors declare that they have no known competing financial interests or personal relationships that could have appeared to influence the work reported in this paper.

Author contributions

Conceptualization: Zhi Zheng, Yipeng Xuan
Formal analysis: Zhi Zheng, Minrui Liu
Investigation: Zhi Zheng, Minrui Liu
Methodology: Zhi Zheng, Wentao Sun, Yipeng Xuan
Supervision: Daolin Du, Qiaorui Si
Writing–original draft: Zhi Zheng
Writing–review & editing: Peng Wang, Daolin Du

Availability of data

Data are available upon reasonable request from the corresponding authors.

References

1. Mohamed MMA, Takaijudin HB, Kutty SRBM, Al-Mahbashi NMY, Al-dhawi BNS, Al-Akwaa HMA. Harnessing the potential of biomass to enhance domestic wastewater treatment through integrated floating wetlands: A review complemented by bibliometric insights. *Results Eng*. 2025;28:108380.

   doi: 10.1016/j.rineng.2025.108380

2. Li S, Gu J, Luo B, Xiao T, Wang Q, Yang C. Integrated biofiltration – gravity-driven membrane system for efficient treatment of shale gas wastewater: Roles of filter media and microbial synergy. *Sep Purif Technol*. 2026;385:136185.

   doi: 10.1016/j.seppur.2025.136185

3. Carnesi M, Mineo A, Amata S, Piccionello AP, Rizzo C, Mannina G. Emerging contaminants in wastewater treatment: the effect of microplastics in an Integrated Fixed-film Activated Sludge (IFAS) Membrane BioReactor (MBR). *Bioresour Technol Rep*. 2025;32:102374.

   doi: 10.1016/j.biteb.2025.102374

4. Zhan H, Ma L, Pan Z, *et al*. Membrane bioreactor strategies for enhanced microplastic removal in wastewater: A review. *J Environ Chem Eng*. 2025;13(6):119999.

   doi: 10.1016/j.jece.2025.119999

5. Bidu JM. Integrated anaerobic reactor and intermittently aerated constructed wetland for enhanced textile wastewater treatment. *Clean Water*. 2025;4:100093.

   doi: 10.1016/j.clwat.2025.100093

6. Kong F, Fu Q, Wang L, Ren HY. Performance optimization and microbial community analysis of integrated anaerobic BES-aerobic MBBR system for azo dye treatment with related wastewater remediation. *Chem Eng J*. 2025;521:166589.

   doi: 10.1016/j.cej.2025.166589

7. Su Q, Zhong Y, Rui JCJ, *et al*. Stability and durability of polymeric membranes in membrane bioreactors for industrial wastewater treatment. *J Environ Chem Eng*. 2025;13(6):120356.

   doi: 10.1016/j.jece.2025.120356

8. Ardic-Demirbilekli R, Korkusuz-Soylu S, Kose-Mutlu B, Koyuncu I. Biofouling mitigation and microbial community dynamics in the quorum quenching membrane bioreactors for industrial wastewater treatment. *J Water Process Eng*. 2025;77:108379.

   doi: 10.1016/j.jwpe.2025.108379

9. Cicekalan B, Shitreh S, Cavdar B, *et al*. Sustainable treatment of dairy industry wastewater using an integrated anaerobic membrane bioreactor-reverse osmosis system for industrial water reuse. *Chem Eng J*. 2025;521:166345.

   doi: 10.1016/j.cej.2025.166345

10. Li H, Xu J, Zhao Y, Lian J. Challenges of precise aeration implementation in conventional wastewater treatment processes: A review. *J Water Process Eng*. 2025;78:108737.

    doi: 10.1016/j.jwpe.2025.108737

11. Xia D, Dou W, Tian Y, *et al*. Efficient removal of nitrogen, phosphorus and antibiotics in freshwater aquaculture wastewater using a novel hybrid aeration biological filter. *J Environ Manage*. 2025;396:128079.

    doi: 10.1016/j.jenvman.2025.128079

12. Pitol CS, Fernandes AT, Menegon CG, *et al*. Enhancing deammonification in a membrane-aerated biofilm reactor:

Intermittent aeration and ammonia loading rate control as key strategies for NOB inhibition in low-strength nitrogen wastewater. *J Water Process Eng*. 2025;79:108861.

doi: 10.1016/j.jwpe.2025.108861

13. Kumalo PC, Amoah ID, Pierneef RE, Ismail A, Bux F, Kumari S. Unveiling the role of aeration systems in the bioaerosol emission rate, particle size and microbial composition from wastewater treatment plants. *J Hazard Mater*. 2025;500:140394.

doi: 10.1016/j.jhazmat.2025.140394

14. Hou S, Xie E, Si B, *et al*. Nanobubble aeration accelerates manure wastewater sanitisation and enhances nitrogen retention while reduces greenhouse gas emissions. *Water Res*. 2026;292:125267.

doi: 10.1016/j.watres.2025.125267

15. Liang J, Xiong H, Hu Z, Xie D, Zhang H, Wan Z. Three-dimensional CFD–PBM insights into bubble dynamics and interfacial momentum transfer in bubble columns. *Sep Purif Technol*. 2026;388:136527.

doi: 10.1016/j.seppur.2025.136527

16. Shah F, Fall I, Zhang D. Breakage and coalescence mechanisms in multiphase flow comprehensive PBM-CFD review with turbulence modelling insights for gas-liquid system. *Int Commun Heat Mass Transf*. 2025;165:109093.

doi: 10.1016/j.icheatmasstransfer.2025.109093

17. Chen Y, Pan Q, Li C, Wang W, Duan J. CFD-PBM numerical simulation and experimental investigation of hydrodynamics in a multistage internal loop reactor with guide cones. *Chem Eng Process - Process Intensif*. 2024;206:110044.

doi: 10.1016/j.cep.2024.110044

18. Shen X, Jia Z, Zhang H, Wang T. Numerical simulation of volumetric mass transfer coefficients in slurry bubble columns with a CFD-PBM coupled model. *Chem Eng Sci*. 2025;318:122153.

doi: 10.1016/j.ces.2025.122153

19. Liu M, Wang M, Zhang K, Yu H. Simulation of synthesizing carbon nanotubes by catalytic chemical vapor deposition in a fluidized bed using a CFD-PBM model. *Powder Technol*. 2025;457:120927.

doi: 10.1016/j.powtec.2025.120927

20. Zang H, Hu S, Liu X, Du W. Applying a CFD-PBM approach to modeling the flow behavior in pressurized bubbling fluidized beds. *Powder Technol*. 2025;452:120541.

doi: 10.1016/j.powtec.2024.120541

21. Na Y, Ranieri L, Di Cesare A, Sabatino R, Vrouwenvelder JS, Fortunato L. Evaluating the removal efficiency of emerging contaminants in a gravity-driven membrane bioreactors GD-MBR under various aeration conditions for primary wastewater treatment. *Case Stud Chem Environ Eng*. 2024;10:100885.

doi: 10.1016/j.cscee.2024.100885

22. Yilmaz T, Demir EK, Başaran ST, Çokgör EU, Sahinkaya E. Impact of aeration on/off duration on the performance of an intermittently aerated MBR treating real textile wastewater. *J Water Process Eng*. 2023;54:103886.

doi: 10.1016/j.jwpe.2023.103886

23. Wang D, Tao J, Fan F, Xu R, Meng F. A novel pilot-scale IFAS-MBR system with low aeration for municipal wastewater treatment: Linkages between nutrient removal and core functional microbiota. *Sci Total Environ*. 2021;776:145858.

doi: 10.1016/j.scitotenv.2021.145858

24. Calderón K, Reboleiro-Rivas P, Rodríguez FA, Poyatos JM, González-López J, Rodelas B. Comparative analysis of the enzyme activities and the bacterial community structure based on the aeration source supplied to an MBR to treat urban wastewater. *J Environ Manage*. 2013;128:471-479.

doi: 10.1016/j.jenvman.2013.05.048

25. Mineo A, Bosco Mofatto PM, Cosenza A, Di Trapani D, Mannina G. Membrane bioreactor operated under intermittent aeration a comprehensive comparison with an IFAS-MBR: A pilot plant experience. *J Environ Chem Eng*. 2025;13(5):118668.

doi: 10.1016/j.jece.2025.118668

26. Di Trapani D, Bosco Mofatto PM, Cosenza A, Mannina G. Attached and suspended biomass kinetics in an IFAS-MBR system operated under intermittent aeration: Long-term monitoring under SRT variation. *J Environ Manage*. 2024;370:122718.

doi: 10.1016/j.jenvman.2024.122718

27. Mehrjoo H, Monfared AEF, Jafari S, Norouzi-Apourvari S, Schaffie M. Simulation of Newtonian and non-Newtonian reactive fluids during the dissolution process in porous media using Lattice Boltzmann method. *Int Commun Heat Mass Transf*. 2026;170:110061.

doi: 10.1016/j.icheatmasstransfer.2025.110061

28. Rapp BE. Conservation of mass: the continuity equation. In: Rapp BE, ed. *Microfluidics*. 2nd ed. Elsevier; 2023:283-289.

doi: 10.1016/B978-0-12-824022-9.00028-0

29. Rapp BE. Conservation of momentum: the Navier-Stokes equation. In: Rapp BE, ed. *Microfluidics*. 2nd ed. Elsevier; 2023:291-309.

doi: 10.1016/B978-0-12-824022-9.00029-2

30. Guo S, Zhang Z, Mei L. Adaptive time-stepping Hermite spectral scheme for nonlinear Schrödinger equation with wave operator: Conservation of mass, energy, and momentum. *J Comput Phys*. 2025;528:113842.

doi: 10.1016/j.jcp.2025.113842

31. Kim JJ, Baik JJ. A numerical study of the effects of ambient wind direction on flow and dispersion in urban street canyons using the RNG k–ε turbulence model. *Atmos Environ*. 2004;38(19):3039-3048.

doi: 10.1016/j.atmosenv.2004.02.047

32. Lopes RJG, Quinta-Ferreira RM. Assessment of CFD Euler–Euler method for trickle-bed reactor modelling in the catalytic wet oxidation of phenolic wastewaters. *Chem Eng J*. 2010;160(1):293-301.

doi: 10.1016/j.cej.2010.03.024

33. Caixeta MP, Marrocos PH, Fernandes IS, Vilar VJP, Santos RJ. A novel Euler-Lagrange approach to simulate gas–liquid mass transfer coefficient (kL) in bubbly flow regimes. *Chem Eng Sci*. 2025;315:121824.

doi: 10.1016/j.ces.2025.121824

34. Yu G, Zhang S, Chen X, Li D, Wang Y. Investigation on aeration efficiency and energy efficiency optimization in recirculating aquaculture coupling CFD with Euler-Euler and species transport model. *J Environ Chem Eng*. 2024;12(5):113927.

doi: 10.1016/j.jece.2024.113927

35. Ren J, Pei Y, Zhou X, Jiao M, Cheng W, Wan T. CFD-PBM simulations the effect of aeration rates on hydrodynamics characteristics in a gas-liquid-solid aerobic fluidized bed biofilm reactor. *Powder Technol*. 2024;443:119963.

doi: 10.1016/j.powtec.2024.119963

36. Zhang H, Guo K, Wang Y, Sayyar A, Wang T. Numerical simulations of the effect of liquid viscosity on gas-liquid mass transfer of a bubble column with a CFD-PBM coupled model. *Int J Heat Mass Transf*. 2020;161:120229.

doi: 10.1016/j.ijheatmasstransfer.2020.120229